Structure of a Thiol Monolayer-Protected Gold Nanoparticle at 1.1 Å Resolution

Pablo D. Jadzinsky, *et al.*

Science **318**, 430 (2007);
DOI: 10.1126/science.1148624

Science (print ISSN 0036-8075; online ISSN 1095-9203) is published weekly, except the last week in December, by the American Association for the Advancement of Science, 1200 New York Avenue NW, Washington, DC 20005.

substrates led to dramatic reduction of fibroblast cell attachment as compared with the unmodified substrates (Fig. 3G and table S3). The polydopamine coating itself was supportive of fibroblast cell adhesion at a level similar to that of bare substrates {for example, the total area of attached cells on 1.08 mm^2 of polydopamine-modified SiO_2 [$(46 \pm 1.4) \times 10^3$ μm^2] was similar to that of unmodified SiO_2 [$(55 \pm 8.6) \times 10^3$ μm^2]}, leading us to conclude that the observed decrease in cell adhesion was due to the grafted mPEG-SH.

Finally, we engineered polydopamine surfaces for specific biomolecular interactions by forming an ad-layer of the glycosaminoglycan hyaluronic acid (HA). HA/receptor interactions are important for physiological and pathophysiological processes, including angiogenesis, hematopoietic stem cell commitment and homing, and tumor metastasis (*31*, *32*). Partially thiolated HA (*33*) was grafted onto a variety of polydopamine-coated substrates (Fig. 4), and HA ad-layer bioactivity was measured via adhesion of the human megakaryocytic M07e cell line. Unlike fibroblasts, M07e cells did not adhere to polydopamine but did adhere to HA-grafted polydopamine surfaces in a dose-dependent manner (Fig. 4B). Together with decreased binding in the presence of soluble HA (Fig. 4C), these findings are consistent with expression of the HA receptor CD44 by M07e cells (fig. S8). Polydopamine and HA-grafted polydopamine surfaces were biocompatible, as evidenced by similar levels of M07e cell expansion as compared with cell expansion on tissue-culture PS surfaces, although only the HA-grafted polydopamine surfaces supported cell adhesion (Fig. 4, D to F, and fig. S9).

We introduced a facile approach to surface modification in which self-polymerization of dopamine produced an adherent polydopamine coating on a wide variety of materials. Polydopamine coatings can, in turn, serve as a versatile platform for secondary surface-mediated reactions, leading ultimately to metal, SAM, and grafted polymer coatings. This two-step method of surface modification is distinctive in its ease of application, use of simple ingredients and mild reaction conditions, applicability to many types of materials of complex shape, and capacity for multiple end-uses.

References and Notes

1. B. D. Ratner, A. S. Hoffman, Eds., *Biomaterials Science: An Introduction to Materials in Medicine* (Elsevier Academic, San Diego, CA, ed. 2, 2004).
2. J.-H. Ahn *et al.*, *Science* **314**, 1754 (2006).
3. P. Alivisatos, *Nat. Biotechnol.* **22**, 47 (2004).
4. R. Langer, *Science* **293**, 58 (2001).
5. J. C. Love, L. A. Estroff, J. K. Kriebel, R. G. Nuzzo, G. M. Whitesides, *Chem. Rev.* **105**, 1103 (2005).
6. G. Decher, *Science* **277**, 1232 (1997).
7. G. Roberts, Ed. *Langmuir-Blodgett Films* (Plenum, New York, 1990).
8. S. R. Whaley, D. S. English, E. L. Hu, P. F. Barbara, A. M. Belcher, *Nature* **405**, 665 (2000).
9. C. Tamerler, M. Sarikaya, *Acta Biomater.* **3**, 289 (2007).
10. D. Y. Ryu, K. Shin, E. Drockenmuller, C. J. Hawker, T. P. Russell, *Science* **308**, 236 (2005).
11. J. H. Waite, M. L. Tanzer, *Science* **212**, 1038 (1981).
12. G. A. Young, D. J. Crisp, in *Adhesion*, K. W. Allen, Ed. (Applied Science, London, vol. 6, 1982).
13. J. H. Waite, X. X. Qin, *Biochemistry* **40**, 2887 (2001).
14. L. A. Burzio, J. H. Waite, *Biochemistry* **39**, 11147 (2000).
15. M. J. Sever, J. T. Weisser, J. Monahan, S. Srinivasan, J. J. Wilker, *Angew. Chem. Int. Ed.* **43**, 448 (2004).
16. M. Yu, J. Hwang, T. J. Deming, *J. Am. Chem. Soc.* **121**, 5825 (1999).
17. H. Lee, N. F. Scherer, P. B. Messersmith, *Proc. Natl. Acad. Sci. U.S.A.* **103**, 12999 (2006).
18. M. Yu, T. J. Deming, *Macromolecules* **31**, 4739 (1998).
19. J. L. Dalsin, B.-H. Hu, B. P. Lee, P. B. Messersmith, *J. Am. Chem. Soc.* **125**, 4253 (2003).
20. A. R. Statz, R. J. Meagher, A. E. Barron, P. B. Messersmith, *J. Am. Chem. Soc.* **127**, 7972 (2005).
21. T. Paunesku *et al.*, *Nat. Mater.* **2**, 343 (2003).
22. C. Xu *et al.*, *J. Am. Chem. Soc.* **126**, 9938 (2004).
23. S. Zürcher *et al.*, *J. Am. Chem. Soc.* **128**, 1064 (2006).
24. Y. Li, M. Liu, C. Xiang, Q. Xie, S. Yao, *Thin Solid Films* **497**, 270 (2006).
25. W. Montagna, G. Prota, J. A. Kenney Jr., *Black Skin: Structure and Function* (Academic Press, San Diego, CA, 1993).
26. C. G. Pierpont, C. W. Lange, *Prog. Inorg. Chem.* **41**, 331 (1994).
27. M. Charbonnier, M. Romand, G. Stremsdoerfer, A. Fares-Karam, *Recent Res. Dev. Macromol. Res.* **4**, 27 (1999).
28. M. J. LaVoie, B. L. Ostaszewski, A. Weihofen, M. G. Scholssmacher, D. J. Selkoe, *Nat. Med.* **11**, 1214 (2005).
29. P. E. Laibinis *et al.*, *J. Am. Chem. Soc.* **113**, 7152 (1991).
30. K. L. Prime, G. M. Whitesides, *J. Am. Chem. Soc.* **115**, 10714 (1993).
31. D. N. Haylock, S. K. Nilsson, *Regenerat. Med.* **1**, 437 (2006).
32. B. P. Toole, *Nat. Rev. Cancer* **4**, 528 (2004).
33. H. Lee, S. H. Choi, T. G. Park, *Macromolecules* **39**, 23 (2006).

34. Single-letter abbreviations for the amino acid residues are as follows: A, Ala; C, Cys; D, Asp; E, Glu; F, Phe; G, Gly; H, His; I, Ile; K, Lys; L, Leu; M, Met; N, Asn; P, Pro; Q, Gln; R, Arg; S, Ser; T, Thr; V, Val; W, Trp; and Y, Tyr.

35. This research was supported by NIH grants DE 14193 and HL 74151. The authors thank T. G. Park and H. Lee for donation of thiolated HA, N. F. Scherer and X. Qu for their generous discussion and technical assistance with TIRF microscopy, and K. Healy for photomask donation. This research used the NUANCE characterization facilities (Keck II, EPIC, and NIFTI) at Northwestern University.

Supporting Online Material

www.sciencemag.org/cgi/content/full/318/5849/426/DC1
Materials and Methods
Figs. S1 to S10
Tables S1 to S3
References

2 July 2007; accepted 12 September 2007
10.1126/science.1147241

Structure of a Thiol Monolayer–Protected Gold Nanoparticle at 1.1 Å Resolution

Pablo D. Jadzinsky,[1,2]* Guillermo Calero,[1]* Christopher J. Ackerson,[1]† David A. Bushnell,[1] Roger D. Kornberg[1]‡

Structural information on nanometer-sized gold particles has been limited, due in part to the problem of preparing homogeneous material. Here we report the crystallization and x-ray structure determination of a *p*-mercaptobenzoic acid (p-MBA)–protected gold nanoparticle, which comprises 102 gold atoms and 44 p-MBAs. The central gold atoms are packed in a Marks decahedron, surrounded by additional layers of gold atoms in unanticipated geometries. The p-MBAs interact not only with the gold but also with one another, forming a rigid surface layer. The particles are chiral, with the two enantiomers alternating in the crystal lattice. The discrete nature of the particle may be explained by the closing of a 58-electron shell.

Nanometer-size metal particles are of fundamental interest for their chemical and quantum electronic properties and of practical interest for many potential applications (*1*, *2*). With the development of facile routes of synthesis (*3*), gold nanoparticles coated with surface thiol layers have been studied in most detail. The particles are typically heterogeneous as synthesized, and though their size distribution may be narrowed by fractionation or other means (*4*–*9*), no atomically monodisperse preparation has been reported, and no atomic structure has been obtained. Electron microscopy (EM) (*10*, *11*), powder x-ray diffraction (PXRD) (*12*), and theoretical studies have led to the idea of Marks decahedral (MD) and truncated octahedral geometries of the metal core, with crystalline packing and {111} faces (*13*). According to this idea, discrete core sizes represent "magic numbers" of gold atoms, arising from closed geometric shells (*14*). Alternatives of amorphous (*15*), molten, or quasimolten (*16*) cores have also been proposed. The structure of the surface thiol layer is similarly obscure. The nature of the gold-sulfur interaction (*17*), the fate of the sulfhydryl proton (*18*), and the conformation of the organic moiety all remain to be determined. The thiols are

[1]Department of Structural Biology, Stanford University School of Medicine, Stanford, CA 94305, USA. [2]Department of Applied Physics, Stanford University, Stanford, CA 94305, USA.

*These authors contributed equally to this work.
†Present address: Department of Chemistry and Biochemistry, University of Colorado, Boulder, CO 80309, USA.
†Present address: Department of Chemistry and Biochemistry, University of Colorado, Boulder, CO 80309, USA.
‡To whom correspondence should be addressed. E-mail: kornberg@stanford.edu

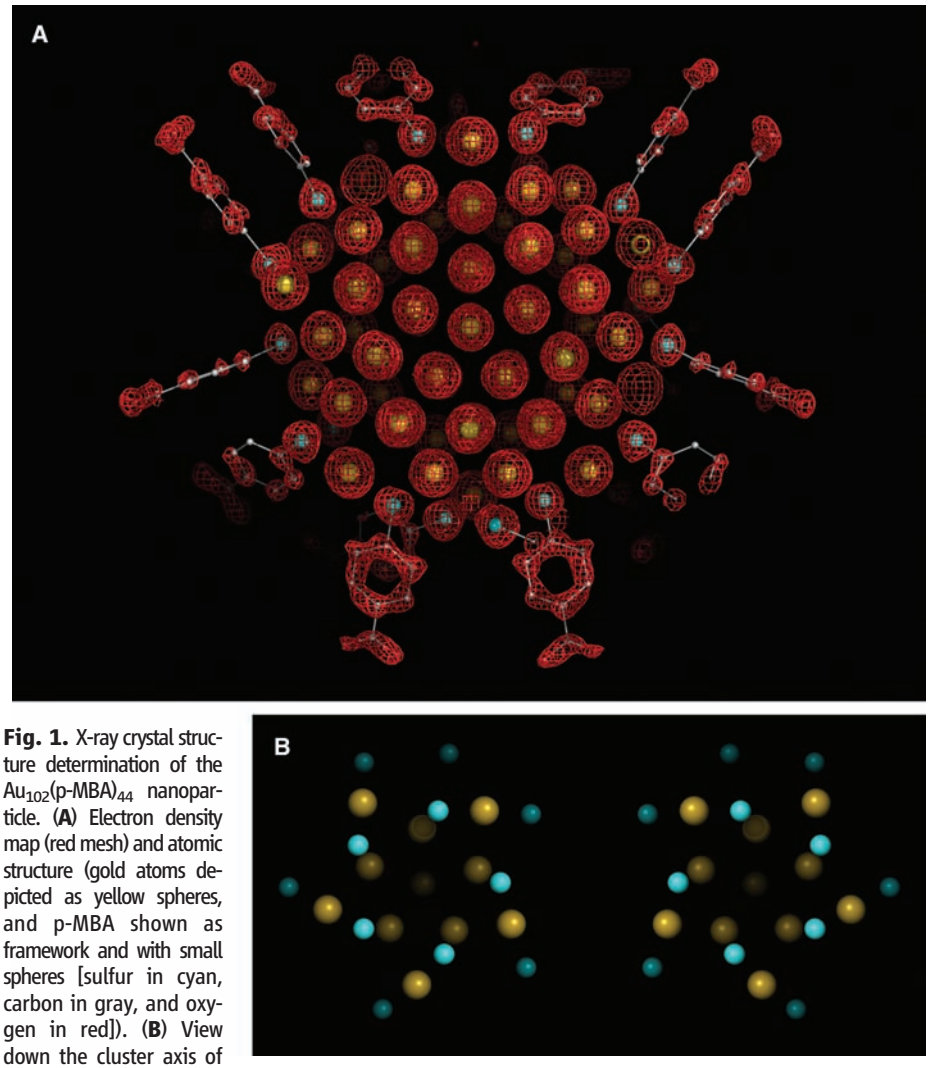

Fig. 1. X-ray crystal structure determination of the $Au_{102}(p\text{-}MBA)_{44}$ nanoparticle. (**A**) Electron density map (red mesh) and atomic structure (gold atoms depicted as yellow spheres, and p-MBA shown as framework and with small spheres [sulfur in cyan, carbon in gray, and oxygen in red]). (**B**) View down the cluster axis of the two enantiomeric particles. Color scheme as in (A), except only sulfur atoms of p-MBA are shown.

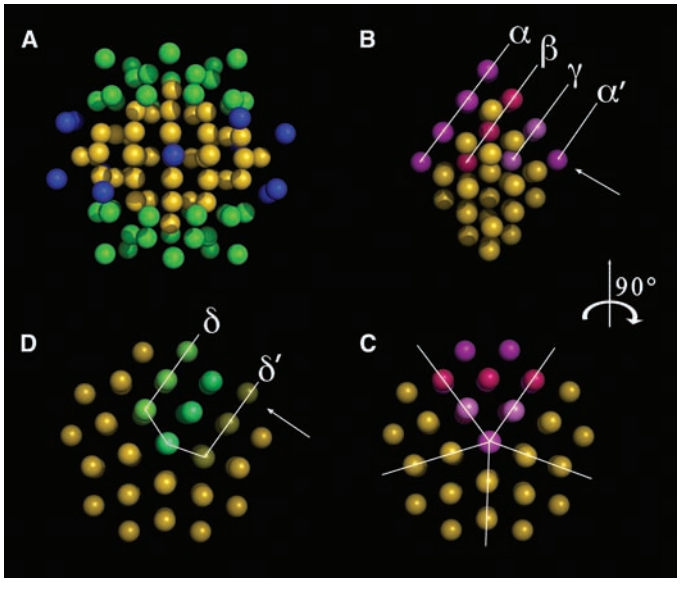

Fig. 2. Packing of gold atoms in the nanoparticle. (**A**) MD (2,1,2) in yellow, two 20-atom "caps" at the poles in green, and the 13-atom equatorial band in blue. (**B**) View of the MD with the axis horizontal, showing the fcc planes (α, β, γ, and α′). When viewed in the direction of the arrow, the fourth plane (α′) overlaps with the first (α), conforming to the definition of fcc planes. (**C**) View of the MD with the axis perpendicular to the page, showing how it may be regarded as five twinned crystals. (**D**) Same view as in (C) but showing hcp crystallites. When viewed in the direction of the arrow, the third plane (δ′) overlaps with the first (δ), conforming to the definition of hcp planes.

exchangeable and presumed to be mobile, further impeding structural analysis (*19*, *20*).

Through systematic variation of solution conditions for gold nanoparticle synthesis, we have obtained particles sufficiently uniform in size for the growth of large single crystals, opening the way to x-ray structure determination. We report here on x-ray analysis of a nanoparticle whose gold core and surface thiol structures differ markedly from what had been anticipated. The gold particles were coated with p-MBA and crystallized from a solution containing 40% methanol, 300 mM sodium chloride, and 100 mM sodium acetate, at pH 2.5 (*21*). The crystals were in the centrosymmetric space group $C2/c$, so diffraction showed no anomalous differences. We obtained initial phases using dispersive differences between data collected at the Au L_{III} edge and a low-energy remote, giving an electron density map that revealed 102 gold atoms and 44 p-MBAs. All electron density was accounted for by the structure (except for solvent water), so the clusters were entirely homogeneous and the numbers of gold atoms and p-MBAs were precise (Fig. 1A). The structure was refined at a resolution of 1.15 Å to R_{work} and R_{free} of 8.8 and 9.5%, respectively. The particles proved to be chiral, with half of an enantiomer in the asymmetric unit of the crystal (Fig. 1B and table S1).

Most gold-gold distances in the core lie in the range 2.8 to 3.1 Å (figs. S1 and S2). The core may be described as a 49-atom MD (2,1,2) with four atoms on the central axis, two 20-atom caps with C_5 symmetry on opposite poles (expanding to 89 the number of gold atoms with fivefold rotational symmetry), and a 13-atom band with no apparent symmetry on the equator (Fig. 2A). Alternatively, the MD may be described as five twinned face-centered cubic (fcc) or hexagonal close-packed (hcp) crystallites (Fig. 2, B to D) (*22*). All 102 gold atoms are found in environments with 12 nearest neighbors—fcc, hcp, icosahedral, or truncated decahedral—except that atoms near the surface lack from 1 to 10 neighbors. The 13 equatorial atoms occupy two different environments, which deviate slightly from local hcp or truncated decahedral (figs. S3 and S4). It is the number and geometry of the equatorial atoms that impart chirality to the core, and the deviations from local symmetry may reflect the interaction of the equatorial atoms with the p-MBA monolayer.

Gold atoms up to 5.5 Å from the center of the particle do not contact sulfur, those in a shell of radius 6.0 to 6.3 Å bind one sulfur, and those in a shell of radius 7.5 to 8.0 Å bind two sulfurs (Fig. 3A and fig. S5). All sulfur atoms lie in a shell of radius 8.3 ± 0.4 Å and bind in a bridge conformation (*23*) to two gold atoms; at least one of the gold atoms binds two sulfurs, forming a "staple" motif (Fig. 3, B and C). The gold-sulfur distance ranges from 2.2 to 2.6 Å (fig. S6). Gold-sulfur-gold angles are 80° to 115°, and sulfur-gold-sulfur angles are 155° to 175° (fig. S7). If the surface is taken as all gold atoms interacting with sulfur, then the coverage by p-MBA (thiol:gold ratio) is 70%, which is much higher than the val-

ues of 31 and 33% for benzenethiol (*24*) and alkanethiols (*17*) on Au(111) surfaces, reflecting the curvature of the nanoparticle surface.

The thiol monolayer is stabilized not only by gold-sulfur bonding but also by interactions between p-MBA molecules. These interactions are of three types: phenyl rings stacked on one another with the centers offset by the ring radius (Fig. 4A), phenyl rings interacting at right angles (T-stacking) (Fig. 4B), and sulfur interacting with a phenyl ring (Fig. 4C). Eighteen of the sulfur atoms are located over the face of a phenyl ring at a distance of about 3.55 ± 0.25 Å, similar to sulfur atoms engaged in aromatic-thiol π hydrogen bonding in proteins (*25*). Almost all sulfur atoms are also engaged in lone pair bonding to a phenyl edge (*25*). Most p-MBAs are linked through chains of such interactions extending from one pole of the nanoparticle to the other (Fig. 4D). This ordering of p-MBAs exemplifies the "self-assembly" of a thiol monolayer on a gold surface (*26*).

The chains of p-MBA interactions extending across the nanoparticle establish the chirality that is apparent from the view of the nanoparticle down the MD axis (Fig. 1B). Most sulfur atoms, bonded to gold atoms in two different shells and to a phenyl ring, are also chiral centers. One enantiomer has 22 sulfur centers with *R* configuration, 18 with *S* configuration, and 2 with no readily assigned chirality, because they are bonded to two gold atoms in the same shell.

The pairing of enantiomeric particles in the crystal demonstrates a surface complementarity of the particles (fig. S8). Interparticle interactions in the crystal thus reflect the chirality of the surface thiol layer. These interactions are of several types. Hydrogen bonding between carboxylic acids occurs at many crystal contacts (fig. S9), in some cases mediated by water molecules (*27*). Such interactions are frequent near the equator, where the phenyl rings extend outward from the particle surface. The p-MBAs from different nanoparticles interdigitate through phenyl-phenyl interactions, especially at the MD poles (fig. S10). Such interactions can explain the common finding that distances between neighboring clusters in two-dimensional gold particle arrays are less than twice the length of the fully extended thiol (*28*, *29*).

The very existence of a discrete $Au_{102}(p\text{-}MBA)_{44}$ nanoparticle is a notable finding from this work. Discrete sizes have been explained in the past by geometrical or electronic shell closing. The arrangement of gold atoms, with polar caps and an equatorial band, argues against geometrical shell closing. If, however, each gold atom ($5d^{10}6s^{1}$) contributes one valence electron, and 44 are engaged in bonding to sulfur, then 58 electrons remain, corresponding to a well-known filled shell. Indeed, a naked cluster in the gas phase containing 58 gold atoms shows exceptional stability (*30*–*32*).

There are several connections of the Au_{102} nanoparticle structure with previous work. First, structures of small gold, silver, and platinum clusters, and of large platinum-palladium clusters, include fivefold symmetry elements and, in one case, also include thiols bridging between pairs of gold atoms (*33*–*36*). Second, EM, PXRD, and theoretical studies of large gold clusters have given results that are consistent with a MD (*10*–*12*). Third, theoretical studies have raised the possibility of distinct gold-sulfur units capping a central gold core (*37*). Fourth, the fcc packing in the core, with a gold-gold distance of 2.8 to 3.1 Å, corresponds with the fcc packing in bulk metallic gold, with a gold-gold distance of 2.9 Å. Fifth, the staple motif, containing alternating gold and sulfur atoms (Fig. 3C), resembles the gold-thiol polymers believed to represent intermediates in the process of nanoparticle formation (*38*). Finally, circular dichroism measurements on gold nanoparticle preparations have shown chiro-optical activity (*39*).

We have screened 15 crystals derived from multiple gold nanoparticle preparations and obtained the same Au_{102} structure, so the unusual arrangement in the 13-atom equatorial band is a consistent result. Other nanoparticle preparations, however, which have also given rise to large single

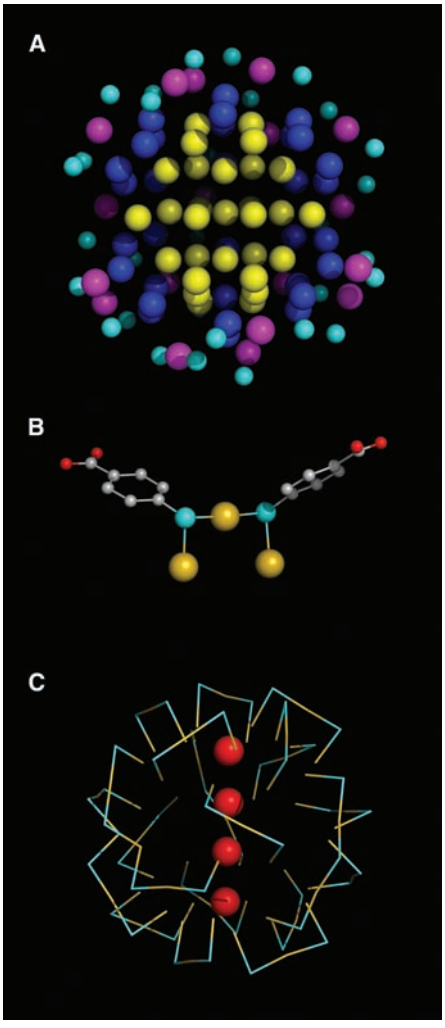

Fig. 3. Sulfur-gold interactions in the surface of the nanoparticle. (**A**) Successive shells of gold atoms interacting with zero (yellow), one (blue), or two (magenta) sulfur atoms. Sulfur atoms are cyan. (**B**) Example of two p-MBAs interacting with three gold atoms in a bridge conformation, here termed a staple motif. Gold atoms are yellow, sulfur atoms are cyan, oxygen atoms are red, and carbon atoms are gray. (**C**) Distribution of staple motifs in the surface of the nanoparticle. Staple motifs are depicted symbolically, with gold in yellow and sulfur in cyan. Only the gold atoms on the axis of the MD are shown (in red).

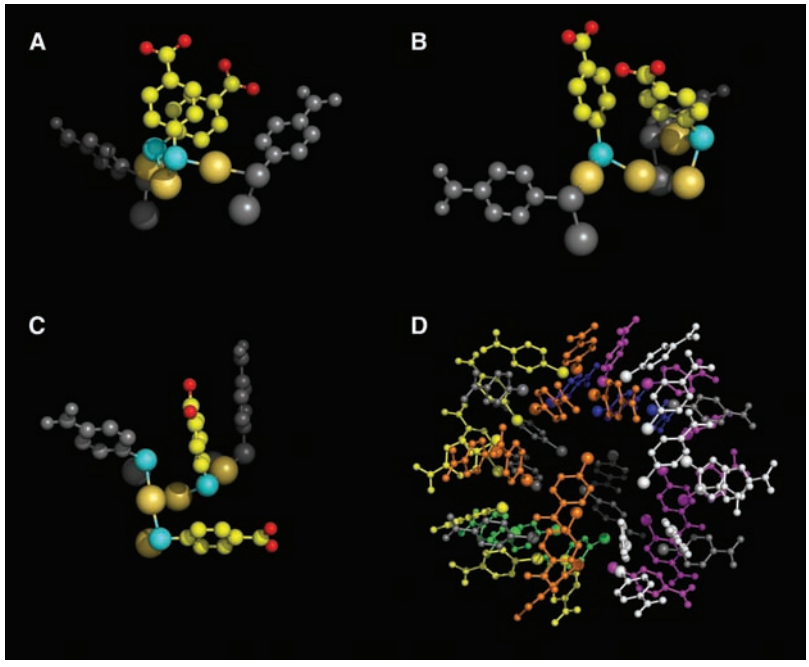

Fig. 4. p-MBA/p-MBA interactions in the surface of the nanoparticle. Color scheme as in Fig. 3B. (**A**) Phenyl rings stacked with faces parallel. (**B**) Phenyl rings stacked edge-to-face. (**C**) Phenyl ring interacting with sulfur. (**D**) Chains of interacting p-MBAs, extending across the surface of the nanoparticle, indicated by a different color for each chain.

crystals, will doubtless reveal other core structures, from which rules or principles of core assembly may ultimately be derived. It remains to investigate the chemical and physical properties of the Au_{102} nanoparticle, as well as to explore the theoretical basis of the gold packing and gold-thiol interactions that we have observed.

References and Notes

1. M. Brust, C. J. Kiely, in *Colloids and Colloid Assemblies*, F. Caruso, Ed. (Wiley-VCH, Weinheim, Germany, 2004), pp. 96–119.
2. M.-C. Daniel, D. Astruc, *Chem. Rev.* **104**, 293 (2004).
3. M. Brust *et al*., *J. Chem. Soc. Chem. Commun.* **1995**, 1655 (1995).
4. J. P. Wilcoxon, P. P. Provencio, *J. Am. Chem. Soc.* **126**, 6402 (2004).
5. J. F. Hicks *et al*., *Anal. Chem.* **71**, 3703 (1999).
6. R. R. Peterson, D. E. Cliffel, *Anal. Chem.* **77**, 4348 (2005).
7. T. G. Schaaff *et al*., *J. Phys. Chem. B* **102**, 10643 (1998).
8. T. G. Schaaff, R. L. Whetten, *J. Phys. Chem. B* **103**, 9394 (1999).
9. B. L. V. Prasad *et al*., *Langmuir* **18**, 7515 (2002).
10. M. J. Yacaman *et al*., *J. Vac. Sci. Technol.* **19B**, 1091 (2001).
11. J. A. Ascencio *et al*., *Surf. Sci.* **396**, 349 (1998).
12. C. L. Cleveland *et al*., *Phys. Rev. Lett.* **79**, 1873 (1997).
13. J. D. Aiken, R. G. Finke, *J. Mol. Catal.* **145**, 1 (1999).
14. T. P. Martin, *Phys. Rep.* **273**, 199 (1996).
15. I. L. Garzon *et al*., *Phys. Rev. B* **66**, 073403 (2002).
16. L. D. Marks, *Rep. Prog. Phys.* **57**, 603 (1994).
17. C. Vericat, M. E. Vela, R. C. Salvarezza, *Phys. Chem. Chem. Phys.* **7**, 3258 (2005).
18. M. Hasan, D. Bethell, M. Brust, *J. Am. Chem. Soc.* **124**, 1132 (2002).
19. R. S. Ingram, M. J. Hostetler, R. W. Murray, *J. Am. Chem. Soc.* **119**, 9175 (1997).
20. A. K. Boal, V. M. Rotello, *J. Am. Chem. Soc.* **122**, 734 (2000).
21. Materials and methods are available as supporting material on *Science* Online.
22. There is a slight difference between an MD and five twinned fcc or hcp crystallites, which is not discernible at the resolution of our analysis.
23. R. Bau, *J. Am. Chem. Soc.* **120**, 9380 (1998).
24. L. J. Wan *et al*., *J. Phys. Chem. B* **104**, 3563 (2000).
25. G. Duan, V. H. Smith Jr., D. F. Weaver, *Mol. Phys.* **99**, 1689 (2001).
26. A. Ulman, *Chem. Rev.* **96**, 1533 (1996).
27. S. Wang, H. Yao, S. Sato, K. Kimura, *J. Am. Chem. Soc.* **126**, 7438 (2004).
28. R. L. Whetten *et al*., *Acc. Chem. Res.* **32**, 397 (1999).
29. M. J. Hostetler *et al*., *Langmuir* **14**, 17 (1998).
30. A. Herlert *et al*., *J. Electron Spectrosc. Relat. Phenom.* **106**, 179 (2000).
31. W. A. de Heer, *Rev. Mod. Phys.* **65**, 611 (1993).
32. T. P. Martin *et al*., *J. Phys. Chem.* **95**, 6421 (1991).
33. E. G. Mednikov, M. C. Jewell, L. F. Dahl, *J. Am. Chem. Soc.* **129**, 11619 (2007).
34. Y. Shichibu, Y. Negishi, *J. Phys. Chem. C* **111**, 7845 (2007).
35. B. K. Teo, H. Zhang, *J. Cluster Sci.* **12**, 349 (2001).
36. B. K. Teo, X. Shi, H. Zhang, *J. Cluster Sci.* **4**, 471 (1993).
37. H. Hakkinen, M. Walter, H. Gronbeck, *J. Phys. Chem. B* **110**, 9927 (2006).
38. A. C. Templeton, W. P. Wuelfing, R. W. Murray, *Acc. Chem. Res.* **33**, 27 (2000).
39. T. G. Schaaff, R. L. Whetten, *J. Phys. Chem. B* **104**, 2630 (2000).

40. We thank R. Whetten for pointing out the possibility of 58-electron shell closing and for other suggestions, G. Sheldrick for help with SHELXL and XPREP, E. Lobkovski for advice on data refinement, and H. Hakkinen, H. McConnell, and C. Chidsey for discussion and for comments on the paper. This work was supported by NSF grant CHE-0617050 and NIH grant AI21144. Portions of this research were carried out at the Stanford Synchrotron Radiation Laboratory (SSRL), a national user facility operated by Stanford University, on behalf of the U.S. Department of Energy (DOE), Office of Basic Energy Sciences. The SSRL Structural Molecular Biology Program is supported by DOE, Office of Biological and Environmental Research, and by NIH, National Center for Research Resources, Biomedical Technology Program, and the National Institute of General Medical Sciences. Portions of this research were conducted at the Advanced Light Source, a national user facility operated by Lawrence Berkeley National Laboratory, on behalf of the DOE, Office of Basic Energy Sciences. The Berkeley Center for Structural Biology is supported in part by DOE, Office of Biological and Environmental Research, and by NIH and the National Institute of General Medical Sciences. GM/CA CAT at the Advanced Photon Source has been funded in whole or in part with federal funds from the National Cancer Institute (Y1-CO-1020) and the National Institute of General Medical Sciences (Y1-GM-1104). Use of the Advanced Photon Source was supported by DOE, Office of Basic Energy Sciences, under contract no. DE-AC02-06CH11357.

Supporting Online Material

www.sciencemag.org/cgi/content/full/318/5849/430/DC1
Materials and Methods
Figs. S1 to S10
Table S1
Structure Parameter Files

1 August 2007; accepted 13 September 2007
10.1126/science.1148624

Constraints on Neon and Argon Isotopic Fractionation in Solar Wind

Alex Meshik,[1]* Jennifer Mabry,[1] Charles Hohenberg,[1] Yves Marrocchi,[1] Olga Pravdivtseva,[1] Donald Burnett,[2] Chad Olinger,[3] Roger Wiens,[4] Dan Reisenfeld,[5] Judith Allton,[6] Karen McNamara,[6] Eileen Stansbery,[7] Amy J. G. Jurewicz[8]

To evaluate the isotopic composition of the solar nebula from which the planets formed, the relation between isotopes measured in the solar wind and on the Sun's surface needs to be known. The Genesis Discovery mission returned independent samples of three types of solar wind produced by different solar processes that provide a check on possible isotopic variations, or fractionation, between the solar-wind and solar-surface material. At a high level of precision, we observed no significant inter-regime differences in $^{20}Ne/^{22}Ne$ or $^{36}Ar/^{38}Ar$ values. For $^{20}Ne/^{22}Ne$, the difference between low- and high-speed wind components is 0.24 ± 0.37%; for $^{36}Ar/^{38}Ar$, it is 0.11 ± 0.26%. Our measured $^{36}Ar/^{38}Ar$ ratio in the solar wind of 5.501 ± 0.005 is 3.42 ± 0.09% higher than that of the terrestrial atmosphere, which may reflect atmospheric losses early in Earth's history.

Planetary materials formed from a disk of gas and dust around the early Sun, which we refer to as the solar nebula. As a standard model, planetary scientists assume that the elemental abundances and especially the isotopic compositions of elements in the nebula are uniform and that the nebular composition is preserved in the solar outer convective zone (*1*). Thus, allowing for relatively well-understood nuclear and physical/chemical isotope fractionation, terrestrial isotopic compositions should be the same as in other solar-system materials. To very high precision, this appears to be true for nonvolatile elements (*1*). However, the standard model fails for the isotopes of O, H, N, and the noble gases where large variations (compared to nonvolatile elements) are observed among terrestrial, lunar, meteoritic (asteroidal), and martian materials (*2*–*4*). Because of the nuclear conversion of D to ^{3}He, solar H is monoisotopic, and $^3He/^4He$ is greatly enhanced. Despite these exceptions, the surface layers of the Sun should preserve the nebular isotopic compositions of C, N, O, and the noble gases (*5*, *6*).

Plasma flowing from the Sun as the solar wind permits the sampling of solar matter. The Apollo Solar Wind Composition (SWC) experiment (*7*) measured relatively precise He, Ne, and Ar isotopic compositions for 1–to–3-day periods in 1969–1972. Here, we address whether the isotopic compositions of Ne and Ar, measured in the solar wind, have changed ("fractionated") from those measured on the surface of the Sun. Ulysses and Advanced Composition Explorer (ACE) spacecraft data have shown that relative proportions of elements in the solar wind are fractionated by amounts correlated with the elemental first ionization potential (FIP) (*8*). FIP fractionation presumably arises because of the preferential extraction of ions relative to atoms during transport into the solar corona from lower levels (*9*). Although the FIP is an atomic property, FIP fractionation models (*9*) predict some isotope effects, but in many specific models, these effects are small. The acceleration of heavier elements from the solar corona into the solar wind can be due to their collisions with protons ("coulomb drag"), and if the drag is incomplete,

[1]Physics Department, Washington University, St. Louis, MO 63130, USA. [2]Division of Geological and Planetary Sciences, California Institute of Technology, Pasadena, CA 91125, USA. [3]Neutron Science and Technology, MS H803, Los Alamos National Laboratory, Los Alamos, NM 87545, USA. [4]Space Science and Applications, MS D466, Los Alamos National Laboratory, Los Alamos, NM 87545, USA. [5]Physics and Astronomy Department, University of Montana, SC 121, 32 Campus Drive, MS 1080, Missoula, MT 59812, USA. [6]NASA/Johnson Space Center (JSC), Mail Code KT, Houston, TX 77058, USA. [7]NASA/JSC, Mail Code KA, Houston, TX 77058, USA. [8]Center for Meteorite Studies, Arizona State University, Mail Code 1404, Tempe, AZ 85287, USA.

*To whom correspondence should be addressed. E-mail: am@physics.wustl.edu